Driving Rate Dependence of Avalanche Statistics and Shapes at the Yielding Transition

Chen Liu,[1,2] Ezequiel E. Ferrero,[1,2] Francesco Puosi,[3,1,2] Jean-Louis Barrat,[1,2] and Kirsten Martens[1,2]
[1]Université Grenoble Alpes, LIPHY, F-38000 Grenoble, France
[2]CNRS, LIPHY, F-38000 Grenoble, France
[3]Ecole Normale Supérieure de Lyon, Laboratoire de Physique CNRS, 46 allée d'Italie, 69364 Lyon Cedex 7, France
(Received 30 June 2015; published 11 February 2016)

We study stress time series caused by plastic avalanches in athermally sheared disordered materials. Using particle-based simulations and a mesoscopic elastoplastic model, we analyze system size and shear-rate dependence of the stress-drop duration and size distributions together with their average temporal shape. We find critical exponents different from mean-field predictions, and a clear asymmetry for individual avalanches. We probe scaling relations for the rate dependency of the dynamics and we report a crossover towards mean-field results for strong driving.

DOI: 10.1103/PhysRevLett.116.065501

Many materials respond to slow driving with strongly intermittent dynamics. Examples include Barkhausen noise in ferromagnets [1–3], stick-slip motion in earthquakes [4], serration dynamics in plasticity of solids [5], and avalanche dynamics in crack propagation [6,7], driven foams [8], and domain wall motion [9].

As in equilibrium critical phenomena, global quantities linked to such bursting collective events are usually power-law distributed and allow for the introduction of scaling functions. In the slow driving limit, the onset of motion can be interpreted as an out-of-equilibrium phase transition, suggesting the existence of families of systems that display similar avalanche statistics. To better identify this universality classes, both experimental [10–17] and theoretical [13,18–21] works have discussed the avalanche "shapes," going beyond the study of scaling exponents.

In deformation experiments of amorphous systems, such as grains, foams, or metallic glasses, avalanche dynamics are typically evidenced in the time series of the deviatoric component of the stress tensor. In the limit of vanishing deformation rate, we approach the so-called "yielding transition." The question of whether or not yielding can be characterized as a continuous dynamical phase transition, belonging to a specific universality class, is still under debate. The analysis of avalanche statistics close to yielding has, therefore, a particular relevance.

In this Letter, we study the emerging yielding dynamics in a simple shear geometry with imposed driving rate. Our focus lies on the shear-rate dependence of the avalanche statistics and thus complements recent quasistatic (QS) studies [22–25]. To address the low shear-rate regime, we use a coarse-graining approach, proven to yield qualitative and quantitative relevant predictions [26–31], and compare the low shear-rate results of our mesoscale model with quasistatic particle-based simulations.

Molecular dynamics (MD).—We consider a mixture of A and B particles interacting via a Lennard-Jones potential: $V_{AB}(r) = 4\epsilon_{AB}[(\sigma_{AB}/r)^{12} - (\sigma_{AB}/r)^{6}]$, with r being the distance between two particles. Units of energy, length, and mass are defined by ϵ_{AA}, σ_{AA} and m_A, the unit of time is given by $\tau_0 = \sigma_{AA}\sqrt{(m_A/\epsilon_{AA})}$. The potential is truncated at $R_c = 2.5$ and a force smoothing is applied between an inner cutoff $R_{\rm in} = 2.2$ and R_c. The two species of particles have equal mass m, but different interaction parameters to prevent crystallization. We set $\epsilon_{AA} = 1.0$, $\epsilon_{AB} = 1.5$, $\epsilon_{BB} = 0.5$, $\sigma_{AA} = 1.0$, $\sigma_{AB} = 0.8$, $\sigma_{BB} = 0.88$, and $m = 1$. The ratio of particles of species A and B is chosen $N_A/N_B = 13/7$ and $8/2$ for $2d$ and $3d$ systems, respectively. Glassy states are obtained (with LAMMPS [32]) by quenching to zero temperature at constant volume systems equilibrated at $T = 1$. An athermal system is achieved by applying to each particle a viscous drag force $\mathbf{F}_{\rm drag} = -\Gamma\mathbf{v}$, where $\mathbf{v}$ is the particle peculiar velocity. We condition the dynamics to be strongly overdamped [22,33] ($\Gamma = 1$). Avalanche statistics are obtained following a quasistatic protocol [22,23]. We impose simple shear at rate $\dot{\gamma} = 10^{-6}$ by deforming the box dimensions and remapping the particle positions. Following Ref. [22], the shear rate $\dot{\gamma}$ is set to zero when a steep increase in kinetic energy occurs (onset of plastic deformation) and only restored when the kinetic energy drops below a threshold.

Elastoplastic (EP) model.—We coarse grain an amorphous medium onto a mesoscopic lattice: each node represents a block of material holding exactly one shear transformation [33–36], for which we assume the same geometry as the globally applied simple shear. To each site i we associate a local scalar shear stress σ_i and a state variable n_i, indicating whether the site plastically deforms ($n = 1$) or not ($n = 0$). Local stresses evolve with the overdamped dynamics:

$$\partial_t \sigma_i = \mu\dot{\gamma} + \mu\sum_j G_{ij}\partial_t \gamma_j^{\rm pl}, \tag{1}$$

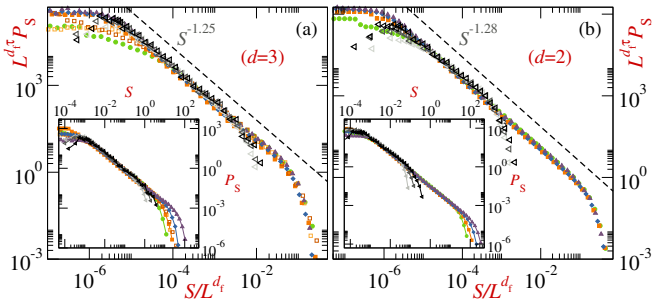

FIG. 1. Stress-drop size distributions. Main panels show rescaled distributions $L^{d_f\tau}P_S$ versus S/L^{d_f} of the EP model compared to MD quasistatic simulations (arbitrary shift applied for the comparison). Insets show not-scaled curves. (a) 3D EP model data for linear system sizes $L = 16$ (green circles), 32 (orange squares), 64 (blue diamonds), 128 (plum triangles), and shear rate 10^{-4} (full symbols). For $L = 32$, $\dot{\gamma} = 10^{-3}$, 10^{-5} are also shown (light and dark orange open squares). Gray scale triangles correspond to quasistatic 3D MD with $L = 40, 60, 80$ (from light to dark). (b) 2D EP data for linear system sizes $L = 256$ (green circles), 512 (orange squares), 1024 (blue diamonds), and 2048 (plum triangles) at $\dot{\gamma} = 10^{-5}$. Gray scale triangles correspond to quasistatic 2D MD with $L = 80, 160, 320$ (from light to dark).

with $\mu = 1$ the elastic modulus, $\dot{\gamma}$ the externally applied shear rate, $\tau = 1$ a mechanical relaxation time, and $\partial_t \gamma_j^{\mathrm{pl}} = n_j \sigma_j/\mu\tau$ the strain rate produced by a plastic rearrangement at site j. G_{ij} denotes the discretized Eshelby propagator [37], which obeys a quadrupolar symmetry in the shear plane with a dipolar long-range character, $G(\boldsymbol{r},\boldsymbol{r}') = \cos(4\theta_{\boldsymbol{r}\boldsymbol{r}'})/|\boldsymbol{r}-\boldsymbol{r}'|^d$. A site yields ($n_i = 0 \to 1$) when its stress reaches a local threshold, $\sigma_i \geq \sigma_i^y$, and recovers its elastic state ($n_i = 1 \to 0$) when a prescribed local deformation increment is attained after yielding, $\int |\partial_t \sigma_i/\mu + \partial_t \gamma_i^{\mathrm{pl}}| dt \geq \gamma_c$. Each time a site yields a new yield stress, σ_i^y is drawn from a distribution of mean σ_0. Model details and parameter choices can be found in Ref. [38] and in the Supplemental Material [39].

Stress-drop statistics and shear-rate dependence.—From the stress-time series we individualize stress drops and define an extensive quantity S proportional to the absolute stress difference multiplied by the system volume. We compare in Fig. 1 the stress-drop distributions P_S in the limit of low $\dot{\gamma}$ for the elastoplastic (EP) model with the quasistatic molecular dynamics (MD) results. In both two (2D) and three dimensions (3D), apart from a plateau regime for small stress drops that depends on shear rate, numerical integration step, and system size, we fit the data using a power law $P_S \sim S^{-\tau} f(S/S_c)$, with f an exponentially decaying cutoff function (exponent definitions in Table I). Noticing that the distributions P_S become independent of $\dot{\gamma}$ in the zero shear-rate limit and in agreement with previous works [23,25], we postulate a system-size-dependent cutoff $S_c \sim L^{d_f}$, with d_f the fractal dimension of the avalanches [23,25,49]. The comparison of these stress-drop statistics with MD results reveals a fair agreement, up to an arbitrary scaling factor related to the difference in simulated length scales.

TABLE I. Measured exponents for the avalanche statistics.

	Expression	EP 2D	EP 3D	$(1/r^2)$ depinning 1D	MF
β	$\dot{\gamma} \sim (\Delta\sigma)^\beta$	1.54(2)	1.55(2)	0.625(5) [50]	2 [51]
τ	$P_S \sim S^{-\tau}$	1.28(5)	1.25(5)	1.25(5) [6,7]	1.5 [52]
d_f	$S_c \sim L^{d_f}$	0.90(7)	1.3(1)	∼1.38 [50]	⋯
τ'	$P_T \sim T^{-\tau'}$	1.41(4)	1.44(4)	∼1.43 [6]	2 [52]
α	$T_c \sim \dot{\gamma}^{-\alpha}$	0.38(4)	0.30(4)	⋯	⋯
z	$T \sim \ell^z$	∼0.57	∼0.82	0.77(1) [50]	⋯
δ	$S \sim T^\delta$	1.58(7)	1.58(5)	∼1.7 [6]	2 [52]
θ	$P_x \sim x^\theta$	0.52(3)	0.37(5)	0	1 [53]

The fitted values of τ for the EP model, both in two and three dimensions ($\tau_{2D} \simeq 1.28$, $\tau_{3D} \simeq 1.25$), compare very well with our and earlier obtained MD results [22,23], are compatible with previous lattice models [54], and lie within error bars of those provided by FEM models [55]. Still, they disagree with what was obtained with quasistatic protocols in cellular automaton models [25] (especially in 3D, where $\tau_{3D}^{QS} \simeq 1.43$), and they contrast even more with the usual mean-field (MF) prediction [52] $\tau^{MF} = 3/2$ (see Ref. [56] for an alternative analysis). The values obtained for d_f ($d_f^{2D} \simeq 0.9$, $d_f^{3D} \simeq 1.3$) are compatible with quasistatic MD simulations, but slightly smaller than those reported in automaton models [25]. They suggest a line geometry of the correlated slip events [24,57], with a modest but clear trend towards a more compact structure in 3D.

Some main results concerning the finite driving rate are summarized in Fig. 2 for the 3D EP model; similar results are found for the 2D case (not shown). The consequences of applying a finite shear rate are twofold [58].

(I) The first important observation is that with increasing driving rate the critical exponents tend towards the mean-field predictions. The yielding exponent β, for example, defined through $\dot{\gamma} \propto (\sigma - \sigma_c)^\beta$, can be derived from the fits in Fig. 2(a) rendering a nontrivial value $\beta \simeq 1.55$ in the low shear-rate regime. For larger shear rates, this value crosses over to $\beta \sim 2$ predicted by the Hebraud-Lequeux model [51]. By sliding a fixed size logarithmic window in $\dot{\gamma}$ (comprising ∼12 points of the main plot data set) and fitting within, we show the resulting $1/\beta$ as a function of the starting position of the window in the inset of Fig. 2(a). Similarly we observe a crossover of the exponents in the steady-state distribution P_x of the local stress excess [53,59], $x_i \equiv \sigma_i^y - \sigma_i$; see Fig. 2(b). Again, in the limit of vanishing shear rates, we observe the curves approaching a shape that initially grows as $P_x \sim x^\theta$, with a nontrivial exponent, as found in the quasistatic case [25,53], attributed to an anomalous random walk process of the local stress with an absorbing boundary condition at $x = 0$ [60]. However, as we increase the shear rate, P_x changes, eventually yielding $\theta \simeq 0$. The driving progressively

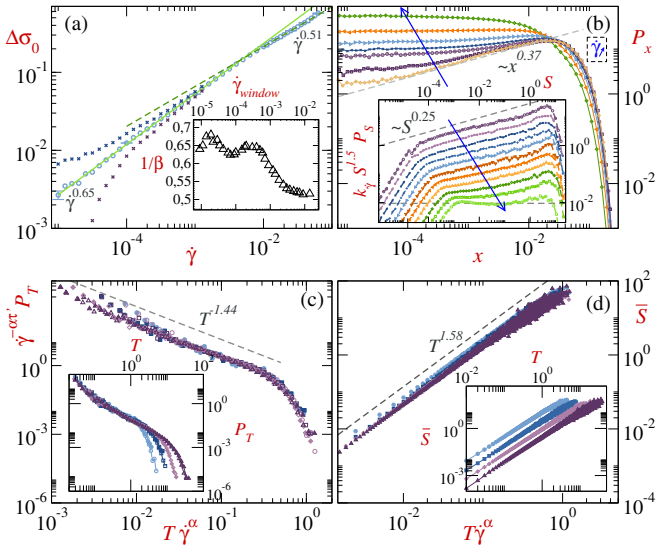

FIG. 2. Shear-rate dependency of the dynamics for the 3D EP model. (a) Log-log plot of $\Delta\sigma_0 \equiv (\sigma - \sigma_c)/\sigma_0$ versus $\dot\gamma$. Circles correspond to the best estimation of $\sigma_c/\sigma_0 = 0.687$, and crosses, to choices of 0.683 and 0.691 instead. Full and dashed lines are power-law fits in selected ranges (extrapolated for comparison). Inset: Crossover of $1/\beta$ as explained in the text. (b) Steady-state distributions P_x of the local distances to threshold $x \equiv \sigma_y - \sigma$ for different shear rates $\dot\gamma \in \{10^{-1.4}, \ldots, 10^{-5}\}$. Inset: Stress-drop distributions for $\dot\gamma \in \{10^{-1}, \ldots, 10^{-3}\}$, rescaled and shifted as explained in the text. Arrows indicate the sense of increasing shear rate. (c) Rescaled distributions of stress-drop duration $\dot\gamma^{-\alpha\tau'} P_T$ versus $T\dot\gamma^{\alpha}$ for $\dot\gamma = 10^{-2}$, 10^{-3}, 10^{-4}, 10^{-5} (from light blue to dark plum, left to right in inset), and system sizes $L = 64$ (closed symbols) and 128 (open symbols). The dashed line shows a law $P_T \sim T^{-1.44}$. Inset: Unscaled data. (d) Average size $\bar S$ for stress drops of the same duration as a function of $T\dot\gamma^{\alpha}$ for $L = 64$ and $\dot\gamma = 10^{-2}$, 10^{-3}, 10^{-4}, 10^{-5}. The dashed line shows $\bar S \sim T^{1.58}$. Inset: Unscaled data, shear rate decreases from left to right.

dominates over the signed kicks from elastic interactions, yielding a biased diffusion of the x's values. This ultimately produces a strictly positive local stress evolution, resembling the x dynamics of the depinning problem [25]. The inset of Fig. 2(b) shows a feature compatible with the shear-rate dependence of P_x and with the β crossover. For different shear rates, we plot $k_{\dot\gamma} S^{1.5} P_S$ versus S, where $k_{\dot\gamma}$ is an arbitrary scaling coefficient to separate the curves and improve visualization. We observe a range of low shear rates where the slope of the transformed distributions is almost unchanged and fully consistent with Fig. 1(a). Above a rate of deformation of about ~0.015, curves progressively flatten, eventually becoming horizontal. Plotting $S^{1.5} P_S$, we show the departure of P_S from the MF expectation $P_S^{\mathrm{MF}} \propto S^{-1.5}$ as the critical point is approached. When investigating the distribution of stress fluctuations $\eta_i = \sum_{j\neq i} G_{ij}(n_j\sigma_j/\tau)$ on each site, we find consistently a change from a peaked distribution with fat tails towards Gaussian-like distributions as we increase the shear rate. We infer from this that the strong correlations at vanishing shear rates (reason for the nontrivial criticality) become negligible for stronger driving, so that the exponents end up being well described by mean-field assumptions.

(II) The second consequence of a finite driving rate is that the critical scaling regime shows not only finite size but also finite shear-rate effects [57,61]. When imposing a finite deformation rate, each stress drop is characterized not only by its magnitude or size S, but also by its duration T. For each stress drop we define a given duration T as the time elapsed between the beginning and the end of the drop. In Fig. 2(c) we present the distributions of durations P_T for a fixed system size and different shear rates. In the probed shear-rate regime we find the dependence on L to be negligible; thus, $P_T(T, L, \dot\gamma) \equiv P_T(T, \dot\gamma)$. The main panel of Fig. 2(c) shows rescaled curves assuming the functional dependence $P_T \sim T^{-\tau'} g(T\dot\gamma^{\alpha})$, with g an exponentially decaying function. We obtain for the 3D case, $\tau'_{3D} = 1.44$ and $\alpha_{3D} = 0.3$. Naturally, we expect the scaling of P_T to be dominated by a growing length scale ξ in the critical limit, where the relations $T \sim \xi^z$ and $S \sim \xi^{d_f}$ hold. Therefore, we expect a scaling relation $S \sim T^{\delta}$ with $\delta = d_f/z$, that we observe over a range of shear rates, yielding the exponent $\delta_{3D} \sim 1.58$ [see Fig. 2(d)], in contrast to the mean field $\delta_{\mathrm{MF}} = 2$. More generally, we observe empirically a power-law scaling of S with T, $\dot\gamma$, and L. Actually, extending the dependencies of the cutoff values in size $S_c = L^{d_f}$ and duration $T_c = \dot\gamma^{-\alpha}$, the mean S at each T should follow $\bar S(T, L, \dot\gamma) = C(L, \dot\gamma) T^{\delta}$, with $C(L, \dot\gamma) \sim L^{d_f} \dot\gamma^{\alpha\delta}$. This relation is fairly verified for the dependence on $\dot\gamma$, illustrated in Fig. 2(d). A rescaling of the size dependence leads to an exponent larger by 15% than d_f estimated from P_S.

Stress-drop shapes.—We address now the analysis of the functional form of the stress drops, i.e., the time evolution of the stress-drop velocity [15–17,52]. In Fig. 3(a) we show rescaled stress-drop velocities V_T (stress-drop shapes) for a 3D system, averaged over drops of the same duration T within the power-law scaling regime of Fig. 2(d). We observe that drops of short duration show a noticeable asymmetric shape, with faster velocities at earlier times. As duration increases, the shape becomes gradually more symmetric. To analyze this asymmetry of stress-drop shapes for different durations, system sizes, and applied shear rates, we fit them with a formula proposed in Ref. [16], $V_T(\tilde t) \propto B[\tilde t(1-\tilde t)]^c [1 - a_s(\tilde t - 0.5)]$ (see also Refs. [15,62]), with B the amplitude of the shape and a_s a parameter quantifying the deviation from a symmetric inverted parabola. We confirm the expected relation $c = \delta - 1$ [recall $S \propto T^{\delta}$ and compare Figs. 3(b) and 2(d)]. In our range of parameters c is almost independent of L and $\dot\gamma$. More relevant for our analysis is the behavior of the fitting parameter a_s [see Fig. 3(b), inset], which shows clearly the crossover from nearly symmetric to asymmetric shapes as we focus on

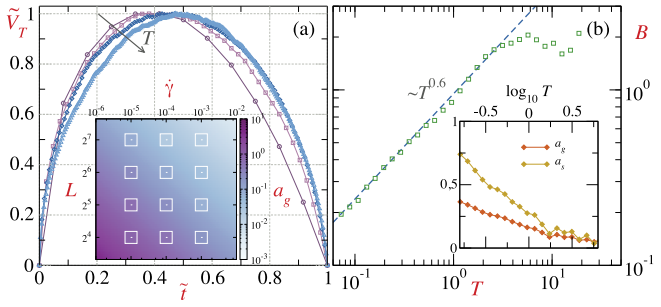

FIG. 3. Stress-drop shape properties for a 3D EP model. (a) Rescaled stress-drop shape $\tilde{V}_T(t) = V_T(t)/\max_t[V_T(t)]$ averaged over stress drops of duration $T \pm \epsilon$, as a function of rescaled time $\tilde{t} = t/T$. From left to right, we show curves at increasing T. Inset: Bordered squares represent fitted values of the asymmetry parameter a_g for different choices of $(\dot{\gamma}, L)$. Color code depicts the fit $a_g = 10^{-0.42} T^{-0.43} \dot{\gamma}^{-0.37} L^{-1.25}$ for $T = 0.5$. (b) Amplitude B of the stress drops versus T, for $L = 32$ and $\dot{\gamma} = 10^{-4}$, as obtained from the fits. The inset shows corresponding $a_s(T)$ and $a_g(T)$ (see text).

shorter durations T. To avoid a fit with various parameters, we use an alternative, purely geometrical measurement of the asymmetry that is relevant even beyond the scaling regime, $a_g = \int_0^1 \{[|V_T(\tilde{t}) - V_T(1-\tilde{t})|]/[V_T(\tilde{t}) + V_T(1-\tilde{t})]\} d\tilde{t}$. When computing $a_g(T)$ for different shear rates at fixed T and L, a_g increases as $\dot{\gamma}$ decreases, whereas for fixed T and $\dot{\gamma}$, a_g decreases as L increases [see inset of Fig. 3(a)]. In the quasistatic limit, where just one independent avalanche occurs at a time, we expect asymmetric stress-drop shapes characterizing individual avalanches. When we increase the driving rate at fixed system size or, equivalently, increase the system size at a fixed rate, we expect stress drops to result from many independent avalanches, since the density of plastic regions is determined and increased by the driving strength [57]. Here, the resulting stress-drop shape draws closer to the mean-field symmetric shape.

Conclusions.—We studied, with a mesoscopic model, the avalanche statistics close to the yielding transition, verifying the relevance of our approach by comparing with particle-based quasistatic simulations. In Table I we summarize the critical exponents obtained for 2D and 3D. Our results clearly reinforce the idea of a nontrivial universality class for the yielding transition, in agreement with earlier findings [23,25,54]. Our estimated exponents confirm within error bars the scaling relations proposed by Lin *et al.* [25]. We also note that our values of τ and τ' are indistinguishable from the exponents expected for the 1D long-range $(1/r^2)$ depinning universality class [6,7]. Although the loading path dependence of the critical exponents remains an open issue, this is an interesting accordance and points towards the role played by the avalanche slip-line geometry.

In the regime of larger shear rates we find that several exponents of the stress-drop statistics draw closer to mean-field predictions. The rise of an increasing number of independent regions with yielding activity (parallel occurring avalanches) justifies the crossover to trivially random statistics. In particular, our data reveal a yielding exponent approaching the prediction of the Hébraud-Lequeux model [51,63,64]. Further, the finite shear-rate protocol allows for the introduction of an additional exponent α that should enter the scaling relations, given $T_c \sim \dot{\gamma}^{-\alpha}$. If we assume a usual scaling scenario, we expect a diverging length scale depending on the distance to the yielding point $\xi \sim (\sigma - \sigma_c)^{-\nu}$, such that $\xi \sim \dot{\gamma}^{-\nu/\beta}$, since $\dot{\gamma} \sim (\sigma - \sigma_c)^{\beta}$. Then, $T_c \sim \xi^z$ yields directly the scaling relation $\alpha = z\nu/\beta$. We have not measured ν, but assuming $\nu = 1/(d - d_f)$ [25] to be valid, we get $\alpha_{2D} = 0.34$ and $\alpha_{3D} = 0.31$, close to our estimated values.

Within the scaling regime for T we observe both asymmetric and symmetric stress-drop shapes depending on system size, shear rate, and duration. This is why we propose to distinguish between individual avalanches (resulting from correlated plastic events) and stress-drop shapes (resulting from many independently occurring avalanches).

The combined study of avalanche size and duration distributions and avalanche shapes has played an essential role in our understanding of the universal aspects of crackling noise and depinning dynamics. With this work, we provide a first numerical prediction of similar quantities in the case of the yielding transition, with a clear indication of a complex non-mean-field behavior. We hope this work will stimulate and provide a benchmark for future experimental studies on systems undergoing a continuous yielding transition, for which detailed data on noise statistics are presently very scarce.

J.-L. B., E. E. F., and C. L. acknowledge financial support from ERC Grant No. ADG20110209. J.-L. B. is supported by IUF. K. M. acknowledges financial support from the ANR Grant No. ANR-14-CE32-0005 (project FAPRES). E. E. F. and J.-L. B. acknowledge the hospitality of the KITP, supported in part by the National Science Foundation under Grant No. NSF PHY11-25915. Most of the computations were performed using the Froggy platform of the CIMENT infrastructure supported by the Rhône-Alpes region (Grant No. CPER07-13 CIRA) and the Equip@Meso project (Reference No. ANR-10-EQPX-29-01). Further, we would like to thank Alexandre Nicolas, Elisabeth Agoritsas, Eric Bertin, Jordi Ortín, and Stéphane Santucci for fruitful discussions, and Mark Robbins and Matthieu Wyart for a useful correspondence.

[1] H. Barkhausen, Phys. Z. **20**, 401 (1919).
[2] G. Durin and S. Zapperi, Phys. Rev. Lett. **84**, 4705 (2000).
[3] G. Durin and S. Zapperi, in *The Science of Hysteresis*, edited by G. Bertotti and I. Mayergoyz (Elsevier, Amsterdam, 2006), pp. 181–267.

[4] A. Ruina, J. Geophys. Res. **88**, 10359 (1983).
[5] Y. N. Dastur and W. C. Leslie, Metall. Trans. A **12**, 749 (1981).
[6] D. Bonamy, S. Santucci, and L. Ponson, Phys. Rev. Lett. **101**, 045501 (2008).
[7] L. Laurson, S. Santucci, and S. Zapperi, Phys. Rev. E **81**, 046116 (2010).
[8] I. Cantat and O. Pitois, Phys. Fluids **18**, 083302 (2006).
[9] V. Repain, M. Bauer, J.-P. Jamet, J. Ferr, A. Mougin, C. Chappert, and H. Bernas, Europhys. Lett. **68**, 460 (2004).
[10] D. C. Chrzan and M. J. Mills, Phys. Rev. B **50**, 30 (1994).
[11] D. Spasojevic, S. Bukvic, S. Milosevic, and H. E. Stanley, Phys. Rev. E **54**, 2531 (1996).
[12] M. C. Kuntz and J. P. Sethna, Phys. Rev. B **62**, 11699 (2000).
[13] S. Zapperi, C. Castellano, F. Colaiori, and G. Durin, Nat. Phys. **1**, 46 (2005).
[14] L. Laurson and M. J. Alava, Phys. Rev. E **74**, 066106 (2006).
[15] S. Papanikolaou, F. Bohn, R. L. Sommer, G. Durin, S. Zapperi, and J. P. Sethna, Nat. Phys. **7**, 316 (2011).
[16] L. Laurson, X. Illa, S. Santucci, K. T. Tallakstad, K. J. Maloy, and K. J. Måløy, Nat. Commun. **4**, 2927 (2013).
[17] J. Antonaglia, W. J. Wright, X. Gu, R. R. Byer, T. C. Hufnagel, M. LeBlanc, J. T. Uhl, and K. A. Dahmen, Phys. Rev. Lett. **112**, 155501 (2014).
[18] J. P. Sethna, K. A. Dahmen, and C. R. Myers, Nature (London) **410**, 242 (2001).
[19] A. P. Mehta, A. C. Mills, K. A. Dahmen, and J. P. Sethna, Phys. Rev. E **65**, 046139 (2002).
[20] P. Le Doussal and K. J. Wiese, Phys. Rev. E **88**, 022106 (2013).
[21] Z. Zhao, X. Ding, J. Sun, and E. K. H. Salje, J. Phys. Condens. Matter **26**, 142201 (2014).
[22] K. M. Salerno, C. E. Maloney, and M. O. Robbins, Phys. Rev. Lett. **109**, 105703 (2012).
[23] K. M. Salerno and M. O. Robbins, Phys. Rev. E **88**, 062206 (2013).
[24] Z. Budrikis and S. Zapperi, Phys. Rev. E **88**, 062403 (2013).
[25] J. Lin, E. Lerner, A. Rosso, and M. Wyart, Proc. Natl. Acad. Sci. U.S.A. **111**, 14382 (2014).
[26] G. Picard, A. Ajdari, F. Lequeux, and L. Bocquet, Phys. Rev. E **71**, 010501 (2005).
[27] D. Rodney, A. Tanguy, and D. Vandembroucq, Model. Simul. Mater. Sci. Eng. **19**, 083001 (2011).
[28] K. Martens, L. Bocquet, and J.-L. Barrat, Phys. Rev. Lett. **106**, 156001 (2011).
[29] M. Talamali, V. Petäjä, D. Vandembroucq, and S. Roux, C.R. Mec. **340**, 275 (2012).
[30] A. Nicolas and J.-L. Barrat, Phys. Rev. Lett. **110**, 138304 (2013).
[31] E. E. Ferrero, K. Martens, and J.-L. Barrat, Phys. Rev. Lett. **113**, 248301 (2014).
[32] S. Plimpton, J. Comput. Phys. **117**, 1 (1995).
[33] F. Puosi, J. Rottler, and J.-L. Barrat, Phys. Rev. E **89**, 042302 (2014).
[34] A. Argon, Acta Metall. **27**, 47 (1979).
[35] A. Tanguy, F. Leonforte, and J.-L. Barrat, Eur. Phys. J. E **20**, 355 (2006).
[36] C. E. Maloney and A. Lemaître, Phys. Rev. E **74**, 016118 (2006).
[37] J. D. Eshelby, Proc. R. Soc. A **241**, 376 (1957).
[38] A. Nicolas, K. Martens, and J. L. Barrat, Europhys. Lett. **107**, 44003 (2014).
[39] See Supplemental Material at http://link.aps.org/supplemental/10.1103/PhysRevLett.116.065501, which includes Refs. [40–48], for a detailed description of the EP model used in the manuscript and explanations of our parallel numerical implementation and post-processing techniques.
[40] G. Picard, A. Ajdari, F. Lequeux, and L. Bocquet, Eur. Phys. J. E **15**, 371 (2004).
[41] E. E. Ferrero, S. Bustingorry, and A. B. Kolton, Phys. Rev. E **87**, 032122 (2013).
[42] NVIDIA Corporation, CUDA C Programming Guide Version 7.0, 2015.
[43] NVIDIA Corporation, CUDA library for the Fast Fourier Transform, DU-06707-001_v7.0, 2015.
[44] J. Hoberock and N. Bell, 2010, http://thrust.github.io/.
[45] J. K. Salmon, M. A. Moraes, R. O. Dror, and D. E. Shaw, in *Proceedings of the 2011 International Conference for High Performance Computing, Networking, Storage and Analysis, 2011 (SC'11)* (Association for Computing Machinery, New York, USA, 2011), pp. 16:1–16:12.
[46] https://bitbucket.org/ezeferrero/epm.
[47] Python Software Foundation. Python Language Reference, version 2.7.6, http://www.python.org.
[48] R. Planet, S. Santucci, and J. Ortín, Phys. Rev. Lett. **105**, 029402 (2010).
[49] N. P. Bailey, J. Schiøtz, A. Lemaître, and K. W. Jacobsen, Phys. Rev. Lett. **98**, 095501 (2007).
[50] O. Duemmer and W. Krauth, J. Stat. Mech. (2007) P01019.
[51] P. Hébraud and F. Lequeux, Phys. Rev. Lett. **81**, 2934 (1998).
[52] K. A. Dahmen, Y. Ben-Zion, and J. T. Uhl, Nat. Phys. **7**, 554 (2011).
[53] J. Lin, A. Saade, E. Lerner, A. Rosso, and M. Wyart, Europhys. Lett. **105**, 26003 (2014).
[54] M. Talamali, V. Petäjä, D. Vandembroucq, and S. Roux, Phys. Rev. E **84**, 016115 (2011).
[55] S. Sandfeld, Z. Budrikis, S. Zapperi, and D. F. Castellanos, J. Stat. Mech. (2015) P02011.
[56] E. A. Jagla, Phys. Rev. E **92**, 042135 (2015).
[57] A. Lemaître and C. Caroli, Phys. Rev. Lett. **103**, 065501 (2009).
[58] To extrapolate our results we assume that the yielding transition is continuous.
[59] M. Müller and M. Wyart, Annu. Rev. Condens. Matter Phys. **6**, 177 (2015).
[60] J. Lin and M. Wyart, Phys. Rev. X **6**, 011005 (2016).
[61] S. Karmakar, E. Lerner, I. Procaccia, and J. Zylberg, Phys. Rev. E **82**, 031301 (2010).
[62] P. L. Doussal and K. J. Wiese, Europhys. Lett. **97**, 46004 (2012).
[63] E. Agoritsas, E. Bertin, K. Martens, and J.-L. Barrat, Eur. Phys. J. E **38**, 71 (2015).
[64] F. Puosi, J. Olivier, and K. Martens, Soft Matter **11**, 7639 (2015).